

Lawrence Berkeley National Laboratory

LBL Publications

Title

Mechanical Characterization of Electrolyzer Membranes and Components Under Compression

Permalink

<https://escholarship.org/uc/item/4jj5p73c>

Journal

Journal of The Electrochemical Society, 171(9)

ISSN

0013-4651

Authors

Arthurs, Claire

Kusoglu, Ahmet

Publication Date

2024-09-02

DOI

10.1149/1945-7111/ad7a26

Copyright Information

This work is made available under the terms of a Creative Commons Attribution License, available at <https://creativecommons.org/licenses/by/4.0/>

Peer reviewed

OPEN ACCESS

Mechanical Characterization of Electrolyzer Membranes and Components Under Compression

To cite this article: Claire Arthurs and Ahmet Kusoglu 2024 *J. Electrochem. Soc.* **171** 094510

View the [article online](#) for updates and enhancements.

You may also like

- [Evaluating the Impact of Cell Assembly and Operating Conditions on the Performance of Anion Exchange Membrane Electrolyzers](#)
Mahmoud Amirsalehi, K Hari Gopi, Pongsarun Satjaritanun et al.
- [Quantum kinetic theory of flux-carrying Brownian particles](#)
Antonio A Valido
- [Bicomplex hamiltonian systems in quantum mechanics](#)
Bijan Bagchi and Abhijit Banerjee

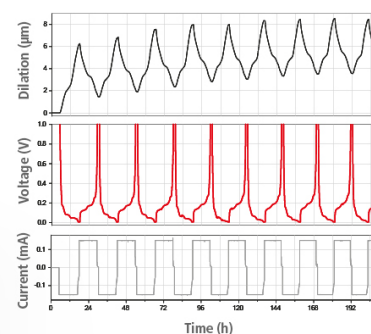
Watch Your Electrodes Breathe!

Measure the Electrode Expansion in the Nanometer Range with the ECD-4-nano.

- ✓ Battery Test Cell for Dilatometric Analysis (Expansion of Electrodes)
- ✓ Capacitive Displacement Sensor (Range 250 μm , Resolution ≤ 5 nm)
- ✓ Detect Thickness Changes of the Individual Half Cell or the Full Cell
- ✓ Additional Gas Pressure (0 to 3 bar) and Temperature Sensor (-20 to 80° C)



EL-CELL[®]
electrochemical test equipment



See Sample Test Results:



Scan me!

Download the Data Sheet (PDF):



Scan me!

Or contact us directly:

+49 40 79012-734

sales@el-cell.com

www.el-cell.com



Mechanical Characterization of Electrolyzer Membranes and Components Under Compression

Claire Arthurs^{1,2}  and Ahmet Kusoglu^{2,z} 

¹Department of Mechanical Engineering, University of California, Berkeley, California 94720, United States of America

²Energy Conversion Group, Lawrence Berkeley National Laboratory, Berkeley, California 94720, United States of America

Proton-exchange membrane (PEM) water electrolysis is a promising technology for producing clean hydrogen by electrochemically splitting water when paired with renewable energy sources. A major roadblock to improving electrolyzer durability is the mechanical degradation of the cell components, which requires an understanding of their mechanical response under device-relevant conditions. However, there is a lack of studies on the mechanical characterization of the PEM and other components, as well as and their interactions. This study aims to address this gap by using a custom-designed testing apparatus to investigate the mechanics of electrolyzer components in uniaxial compression at 25 and 80 °C. Findings show stress-strain response of components have a varying degree of nonlinearity owing to their distinct deformation mechanisms and morphologies, from porous structures to polymers. These results are used to develop an expression for compressive stress-strain response of Nafion membranes and then analyze the deformation of components under applied pressure by using a 1-D spring network model of cell assembly. This work provides a new understanding of mechanical responses of the electrolyzer membrane and cell components, which can help assess material design and cell assembly strategies for improved electrolyzer durability.

© 2024 The Author(s). Published on behalf of The Electrochemical Society by IOP Publishing Limited. This is an open access article distributed under the terms of the Creative Commons Attribution Non-Commercial No Derivatives 4.0 License (CC BY-NC-ND, <http://creativecommons.org/licenses/by-nc-nd/4.0/>), which permits non-commercial reuse, distribution, and reproduction in any medium, provided the original work is not changed in any way and is properly cited. For permission for commercial reuse, please email: permissions@iopublishing.org. [DOI: 10.1149/1945-7111/ad7a26]



Manuscript submitted May 5, 2024; revised manuscript received September 2, 2024. Published September 25, 2024.

Supplementary material for this article is available [online](#)

A growing need for carbon-free hydrogen as an energy carrier and fuel in many transportation and industrial applications necessitates the development and deployment of electrolytic hydrogen generation from renewable electricity.¹ Proton-exchange membrane (PEM) electrolyzers are an emerging technology for carbon-free hydrogen generation when powered by renewable energy. However, performance, cost, and durability are significant areas needing improvement for large-scale commercial deployment of water electrolyzers. In particular, the lifetime of PEM electrolyzers must be improved to meet the 2026 Department of Energy target of 80,000 h.² A few studies reported achievable lifetimes of up to 60,000 h but with higher catalyst loadings than the current DOE targets.^{3,4} Demonstrating such lifetimes with the current state of materials is still an ongoing challenge as identified in the DOE's H2NEW consortium - Hydrogen from Next-generation Electrolyzers of Water (H2NEW).⁵

A critical component affecting the electrolyzer durability is the PEM which suffers from a combination of chemical degradation and mechanical damage during operation.⁶⁻⁹ Additional stressors arise during the cell assembly as the membrane is compressed between other cell components and constrained at the edges of the membrane electrode assembly (MEA). An important pathway to understand component response and interaction during assembly and cell operation is to characterize their mechanical response in device relevant conditions, particularly under compression, considering the growing interest in developing effective assembly strategies and differential pressure operation in next-generation electrolyzers. Common membrane failures resulting in reduced performance are decomposition from chemical attack by hydroxide radicals, delamination between the membrane and electrodes due to membrane thinning or creep, intrusion from GDL and PTL fibers, and crack formation near the gaskets due to increased stress and constraints.^{6,7,10-15} Therefore, it is imperative to mitigate failures associated with mechanical degradation from assembly or operation. An effective cell assembly strategy is critical to enhance the cell performance and mitigate chemical and mechanical damage.^{5,15-17} To better predict component lifetimes, a detailed analysis of cell

components' mechanical response under device configuration is necessary.⁶ While such analysis and design strategies have been employed for membranes in PEM fuel cells,¹⁸⁻²³ these investigations are not fully extended to electrolyzers. Previous studies modeled fuel cell systems which have different materials and operating conditions than electrolyzers impacting the mechanical response of the cell components. This study addresses this gap by focusing on the electrolyzer materials and operating conditions (compression in liquid water, at 80 °C).

The components assessed in this study include the PEM, the gas diffusion layer (GDL), the porous transport layer (PTL), the gasketing material, and a polymer used as edge protection. The prototypical chemistry for PEMs is a sulfonated fluoropolymer, perfluoro-sulfonic acid (PFSA).²⁴ H2NEW consortium adopted standardized materials for the electrolyzer cell MEA (so-called, Future Generation Membrane Electrode Assembly or "FuGeMEA").⁵ The components of a FuGeMEA consist of a NafionTM 115 PEM (N115), a Pt/C cathode catalyst layer, IrO₂ anode catalyst layer, cathode GDL (AvCarb MGL280) at approximately 20% compression, and a Pt-coated titanium felt anode PTL (Bekaert 2GDL10N, 56% nominal porosity).²⁵ A common gasketing material is polytetrafluoroethylene (PTFE). Kapton[®] HN, a polyimide film, is being considered for edge protection within an electrolyzer cell due to its thermal, chemical, and mechanical stability, which could prevent damage to the membrane at the diffusion media and gasket interface.

These components' mechanical properties are directly related to the mechanical durability of the cell assembly, yet their mechanical behavior has not been characterized systematically, let alone under compression. The tensile properties of PFSA have been extensively characterized in literature.²⁶⁻³¹ However, there has been little investigation into the compression response of PFSA (or other electrolyzer cell components for that matter) under device-relevant conditions due to the difficulty of conducting compression experiments on thin membranes (<200 micron) while under hydration. There have been a few studies that overcame these challenges by developing a custom-designed mechanical testing apparatus and procedure to investigate PFSA response under compression however, they are limited to lower temperatures.^{22,32,33} It is of interest to characterize these materials under compression, and at higher temperatures to mimic electrolyzer operation (80 °C).^{6,8,17,34} The

^zE-mail: akusoglu@lbl.gov

mechanical response of PFSA, is expected to change at these temperatures approaching its glass transition temperature (90–110, depending on hydration level).²⁴ Since the mechanical response of PFSA under compression differs greatly than from tension, as reported in our previous work,³³ it is critical to characterize membranes and other cell components under compression and at elevated temperatures.

Polytetrafluoroethylene (PTFE) exhibits rate- and temperature-dependent mechanical response, which has been extensively studied and many constitutive models have been developed.^{35,36} Similarly, the mechanical properties of polyimide films (Kapton) have been characterized in tension and are also temperature and strain rate dependent.^{37,38} In fuel cell literature, GDLs have been the focus of several compression-based studies driven by the need for better inter-component contact, water transport, and reduced resistance to improve fuel cell performance.^{14,39–48} However, excessive compression of GDLs may reduce the mass flow rate of reactants and therefore limiting the current.^{14,39–42,48} Existing models for fibrous materials were used to develop a stress-density constitutive model to predict the mechanical behavior of the GDL under compression by taking into account material density and mechanical history.^{43,49} The orthotropic elastic properties of various GDLs were characterized through tensile, shear, and compression tests.⁴⁴ The GDL stress-strain response was found to change depending on the GDL structure^{47–49} as well as the rib/channel configuration of the cell.⁴⁵

In the field of electrolysis, sintered powder titanium PTLs have been tested mechanically, although under tension.^{50,51} Beyond the electrolyzers, compression studies have been conducted on the mechanical behavior of porous or foam metals which have similar microstructure to the titanium felt used in electrolyzer cells.^{52–54} The mechanical properties of such materials are dependent on the raw material, sintering parameters, and morphology (e.g., pore size, porosity). In studies focused on sintered powdered titanium foams, titanium scaffolds were mechanically tested under compression and modulus was found to decline with increasing porosity⁵² and exhibit a rate-dependent response.⁵³ The compressive response of sintered fiber metal sheets for other applications have also been investigated with micro tomography to assess deformation mechanisms within metal fiber structures.⁵⁴ Nevertheless, the compression response of titanium fiber PTLs for electrolyzers have not been studied under compression. Yet, recent electrolyzer studies on PTLs, GDLs, and their interfacial structure have highlighted the need for such mechanical understanding of system components.^{6,55,56}

In addition to determining the properties of individual components, the mechanical behavior of their assembly is significant for electrolyzers. There have been few research efforts to assess the PFSA membrane and component interfacial interactions within an electrolyzer cell. In an X-ray tomography of catalyst-coated membranes and porous layers, the water uptake and resistance was found to decrease under the land regions due to clamping forces.⁵⁷ By varying the cell design to adjust the CCM compression, the increase in mass transport losses was attributed to a reduced pore volume in the GDL which diminished removal of dissolved hydrogen.³⁴ Thus, understanding and mitigating the mechanical failure of electrolyzer components and their assembly requires a systematic examination of

their mechanical properties. This study elucidates the mechanical response of electrolyzer cell components under quasistatic compression at low and elevated temperatures, and under hydration for membranes, and aims to improve the understanding of the mechanical interactions between cell components. Further, the constitutive response of PFSA under compression with varied environmental conditions is modeled using experimental data. Finally, the acquired mechanical properties are used to analyze the compression of the cell components under an applied assembly stress with a simplified 1-D mechanical spring network representation.

Experimental Methods

Materials.—The components of a FuGeMEA consist of Nafion 115 membrane (N115), a Pt/C cathode catalyst layer, IrO₂ anode catalyst layer, cathode gas diffusion layer (AvCarb MGL280) (GDL) at approximately 20% compression, and a Pt-coated titanium felt anode porous transport layer (PTL, Bekaert 2GDL10N, 56% nominal porosity). Grade II titanium is commonly used for the flow plates or end plates and PTFE and Kapton, a polyimide film, are used as gasketing and edge protection, respectively. Table I provides a list of the electrolyzer components used in this study.

Mechanical testing.—All cell components were individually tested under uniaxial compression to assess mechanical behavior and determine compressive properties using a custom-made compression apparatus (Fig. 1). The testing setup is inspired from previous studies^{33,60} and improved by incorporating heating control. The modified setup has a liquid water chamber, two heating bands from Omega, and two K-type thermocouples connected to a temperature control system (Digi-Sense 2-Zone Temperature Controller) and is attached to an Instron 68TM-10 Dual Column Tabletop Testing System. The temperature is verified with an external temperature data logger from National Instruments. The compression apparatus is made of stainless steel and equipped with a DP/2/S Orbit 3 Digital Gage Probe as the linear variable displacement transducer (LVDT) capable of recording displacement at 0.01 μm resolution.

First, circular samples were cut to 6.35 mm diameter for compression testing by either laser (in the case of titanium PTL) or using a circular die and rubber mallet. Sample thickness was measured using a Heindenhan depth probe, and diameter measurements were taken optically with a goniometer after calibration with a Mitutoyo gauge block. Measurements were taken at three locations for each thickness and diameter then averaged. For hydrated membrane samples (e.g., Nafion), the sample was placed on a porous ceramic disc that is housed by the water reservoir of the fixture. Then, a piston connected to the LVDT was placed on the sample. Once the sample was positioned and aligned, the water reservoir of the fixture was filled with Millipore-grade water (18.2 M Ω *cm). The change in thickness of the membrane sample was monitored until a steady-state thickness is reached. For non-hydrated tests carried out in ambient conditions (40%–50% RH), dry samples were placed on a stainless-steel disk. Dry samples were not stored or soaked in liquid water; hydrated samples of PFSA were stored in purified liquid water.

Table I. List of electrolyzer components and their properties investigated in this study.

Component	Material	Nominal thickness	Notes and references
PEM	Nafion 115	125 μm	58
Porous Transport Layer (PTL)	Bekaert 2GDL10N	254 μm	
Edge Protection	Kapton [®] HN	1 mil (25.4 μm)	
Gasket	Skived PTFE	10 mil (254 μm) standard 9 mil (228.6 μm) edge protection	
Gas Diffusion Layer (GDL)	MGL280	280 μm	at 50 kPa ⁵⁹
Flow Plate	Grade II Ti	1 inch (25400 μm)	

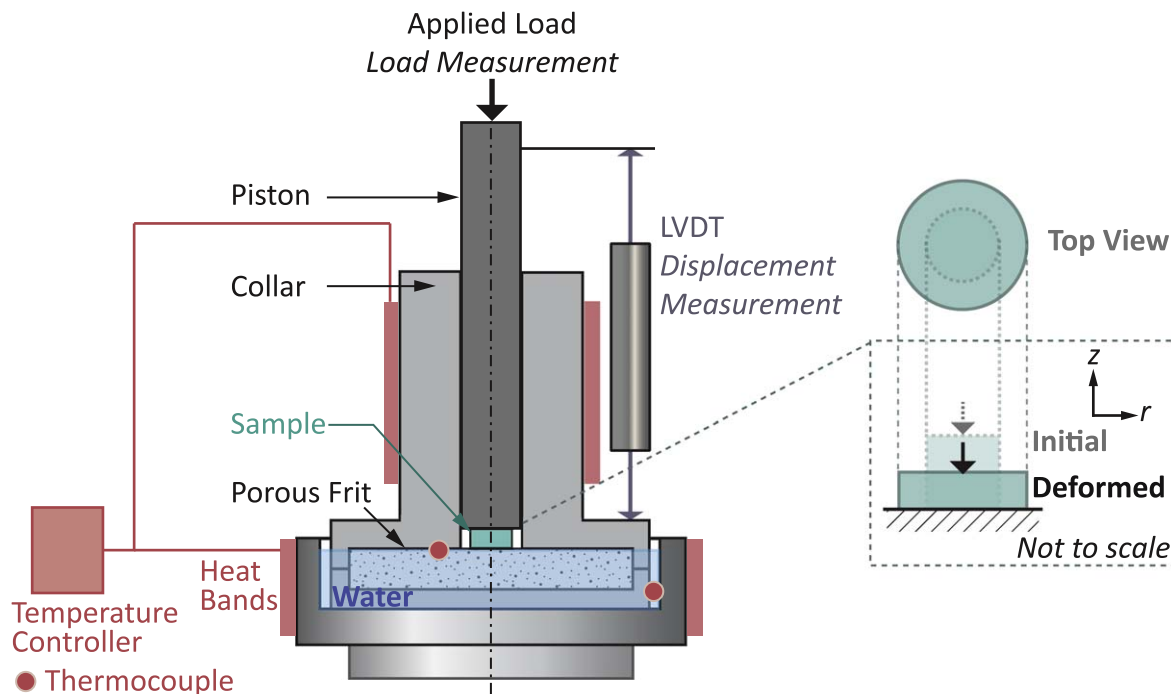


Figure 1. Custom-designed mechanical compression apparatus with temperature control and water reservoir.

The temperature controller was then switched on and the apparatus and membrane were allowed to heat and equilibrate for about 30 min, while the displacement was continuously recorded. Finally, the equilibrated sample was compressed at a rate of $10 \mu\text{m min}^{-1}$ up to 40 MPa of compressive stress (400 bar, $\sim 5,800$ psi), and then the load was removed at the same rate. The strain rate was chosen for a relatively slow loading to achieve a quasistatic response. A preload of 5 N was applied before the experiment began to ensure uniform contact between the sample surface and apparatus. Thickness and diameter measurements of the post-compressed samples were taken again in the same manner as was done before the testing began. This technique allows in situ measurement of the

compressive response of the membrane in liquid water, at a fixed temperature. Repeated experiments for all materials at 25°C were conducted to validate the procedure (see supplementary information for details).

In this study, mechanical response is generally represented using engineering (nominal) stress and strain, which are calculated from the applied load divided by the measured original cross-sectional area and the displacement divided by the measured original sample length, A_o and L_o , respectively, in the direction of the applied load, respectively:

$$\sigma_{\text{eng}} = \frac{F}{A_o} \quad [1]$$

$$\varepsilon_{\text{eng}} = \frac{L_i - L_o}{L_o} = \frac{\Delta L}{L_o} \quad [2]$$

Swelling measurements.—To verify hydration of the membrane, the compression apparatus and the LVDT are used to measure the out-of-plane swelling during the temperature ramp. The sample is first measured at room temperature and thickness change is monitored with the LVDT before load is applied and while the sample is heated to 80°C . The standard deviation of the room temperature measurements is added to the equipment error from the LVDT for the heated sample.

Analysis of mechanical compression.—Quantifying the toughness, energy dissipation, and stiffness of each component can provide greater insight into the deformation mechanisms. Various mechanical properties can be determined from the engineering stress-strain response, as shown in Fig. 2 for the case of hydrated, room temperature PFSA membrane. The area under the loading curve is toughness (sometimes referred to as modulus of toughness), which is the amount of strain energy per unit volume (strain energy density). Toughness is an indicator of material ductility under tension since it characterizes a material's ability to deform until failure, which, however, does not apply to compression. Because in this study, the materials are compressed without failure, strain energy density is calculated from the stress-strain regime (stress

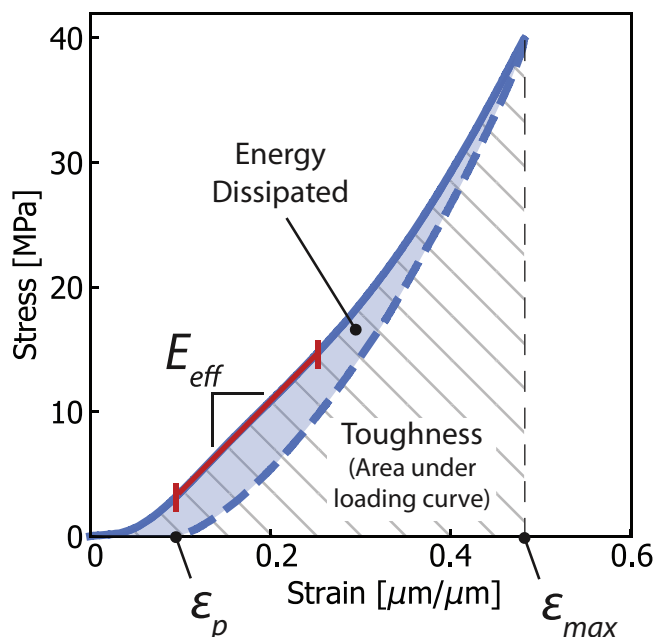


Figure 2. Determination of effective modulus, dissipated energy, toughness, plastic strain (ε_p), and strain at 40 MPa applied stress (ε_{max}) on load-unload stress-strain curve for hydrated N115 at 25°C .

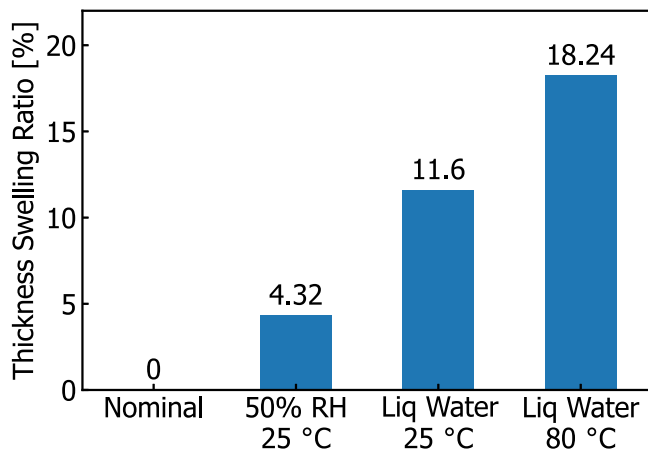


Figure 3. Calculated swelling ratio based on measured thickness with respect to the nominal thickness (See SI for additional information).

up to 40 MPa and strain up to ϵ_{\max}) which serves as a proxy for toughness. The area between loading and unloading curves (shaded in Figs. 2 and in 4) is the energy dissipated, or hysteresis, as internal friction or heat during deformation. The magnitude of strain at the end of unloading (at zero stress) is the plastic strain (ϵ_p), which is indicative of permanent deformation induced during the compression.

Because all the material responses to uniaxial compression are nonlinear and contain plasticity in this study, a typical material property description of elastic modulus or Young's modulus as it is done in tension is not applicable. For this reason, a secant modulus is calculated for each material. Additional details on the secant modulus analysis can be found in the SI.

Results and Discussion

Hydration state in membrane.—The hydration of PFSA membrane is a key factor in both the ionic conductivity (performance) and the mechanical response to an applied stress.²⁴ Therefore, it is helpful to verify the hydration state of the membrane during the compression tests. Figure 3 shows the change in measured thickness of N115 samples with hydration (from nominal dry thickness to equilibrated in water at 25 and 80 °C). The amount of water in a hydrated membrane is commonly defined as water content^a, Λ_w , which is defined as the amount of water per SO_3^- group:

$$\Lambda_w \equiv \frac{\text{mol}(\text{H}_2\text{O})}{\text{mol}(\text{SO}_3^-)} = \left(\frac{\Delta M_w}{M_p} \right) \frac{EW}{\bar{M}_w} \quad [3]$$

where M_w (M_p) and \bar{M}_w (\bar{M}_p) are the mass and molar mass of water (dry polymer), respectively. Equivalent weight (EW) is the ratio of the mass of polymer to the moles of ionic group, in this case SO_3^- .

The volumetric change can be related to the swelling strain, ϵ_{swell} , and therefore one-dimensional change in thickness assuming isotropic swelling in the following expression:

$$\begin{aligned} \epsilon_{\text{swell}} &= \left(1 + \frac{\Delta L}{L_o} \right)^3 = \frac{V_{\text{swell}}}{V_{\text{dry}}} = \frac{V_p + \Delta V_w}{V_p} \\ &= 1 + \frac{\Delta V_w}{V_p} = 1 + \frac{\Delta \Lambda_w \bar{V}_w}{\bar{V}_p} \end{aligned} \quad [4]$$

where V_w (V_p) and \bar{V}_w (\bar{V}_p) is the volume and molar volume of water (dry polymer), respectively. The molar volume of water is defined as:

$$\bar{V}_w = \frac{\bar{M}_w}{\rho_w} \quad [5]$$

The molar mass and density of water (ρ_w) are 18 g mol^{-1} and 1 g cm^{-3} , respectively. The molar volume of Nafion is defined as:²⁴

$$\bar{V}_p = \frac{EW}{\rho_p} \quad [6]$$

The equivalent weight of Nafion 115 is taken to be $1100 \text{ g}_{\text{polymer}}/\text{mol}_{\text{ionic-group}}$ and the density of dry polymer is 2.1 g/cm^3 .²⁴ From Fig. 2, the $\Delta L/L_o$ at 80 °C is 0.18 with respect to initial state of the membrane at nominal thickness of 125 micron. This corresponds to a change in water content of $\Delta \Lambda_w = 18.9$ for N115 at 80 °C, which is close to the literature values of approximately 21 ± 1 , which includes the residual bound water in membranes that exist at nominal thickness.²⁴ At 25 °C, the calculated water content at 50% RH is 3.9 using a swelling strain of 4.3%, which also agrees with published literature values of 4.²⁴ This confirms the relative changes in the hydration state of the polymer membrane based on the measured thickness swelling.

Stress-strain response of components.—The stress-strain response of the electrolyzer cell components under uniaxial compression (through-plane direction) and controlled environments are useful for understanding the material response and determining relevant material properties. Compressive mechanical response of PFSA, PTL, GDL, polyimide film (Kapton), and PTFE in thickness direction are summarized at 25 and 80 °C (Figs. 4 and 5). All samples exhibit a stress-strain response with a varying degree of nonlinearity due to their polymeric morphology (e.g., PFSA) or porous microstructure (e.g., PTL and GDL). Elevated temperature has minimal impact on the stress-strain response of the GDL, PTL, and Kapton but has a noticeable softening effect in PFSA and PTFE.

Dry PFSA membrane, which herein refers to Nafion 115 in ambient conditions, exhibits a linear stress-strain response under compression (Fig. 4a). Wet PFSA membrane exhibits a nonlinear response (Fig. 4b). Both dry and hydrated membranes lack a discernible yield point commonly associated with a transition from linear to nonlinear regime.^{27,28,31,61} Yielding in tension is commonly observed following an initial linear elastic response and previously reported for dry PFSA, whereas for liquid-equilibrated PFSA, the yield point becomes less apparent due to reduced stiffness.^{26–28} Because, with hydration, growing water domains in PFSA polymer matrix reduce the fraction of hydrophobic domains that lower the effective stiffness.^{24,62,63} With increased temperature, further softening of the stress-strain response is observed (Fig. 5).

While it is not trivial to assess plasticity from these nonlinear loading curves due to the lack of a transition point that can be attributed to a yield stress, one can infer the degree of the permanent deformation from the unloading curves, that is the strain at zero stress at the end of the loading (Fig. 5). This final strain value can be attributed to a plastic strain. The hydrated PFSA has greater induced plasticity (9% strain) than dry PFSA (3% strain). Since the original sample thickness for the hydrated case includes the swelling from water uptake, the greater magnitude of permanent strain in the hydrated case could partially be due to the water being compressed out of the membrane sample at these high loads as it has been shown that water uptake decreases with increased compressive stress.²² However, since the membrane could re-equilibrate with water upon unloading, any final reduction in thickness upon load removal likely arises from permanent deformation.

PTFE is used as the gasketing material in electrolyzer cells and is also the chemical backbone of the PFSA imparting its chemical and mechanical stability.²⁴ Thus, it is not surprising that PTFE displays a stress-strain curve qualitatively similar to dry PFSA, but with a stiffer response owing to its higher crystallinity ($\sim 70\%$ ^{64,65}) when compared with PFSA (7%-17% for extruded membranes²⁴). At

^aWater content is usually denoted with a lowercase lambda but to distinguish water content from stretch, a capital lambda is used.

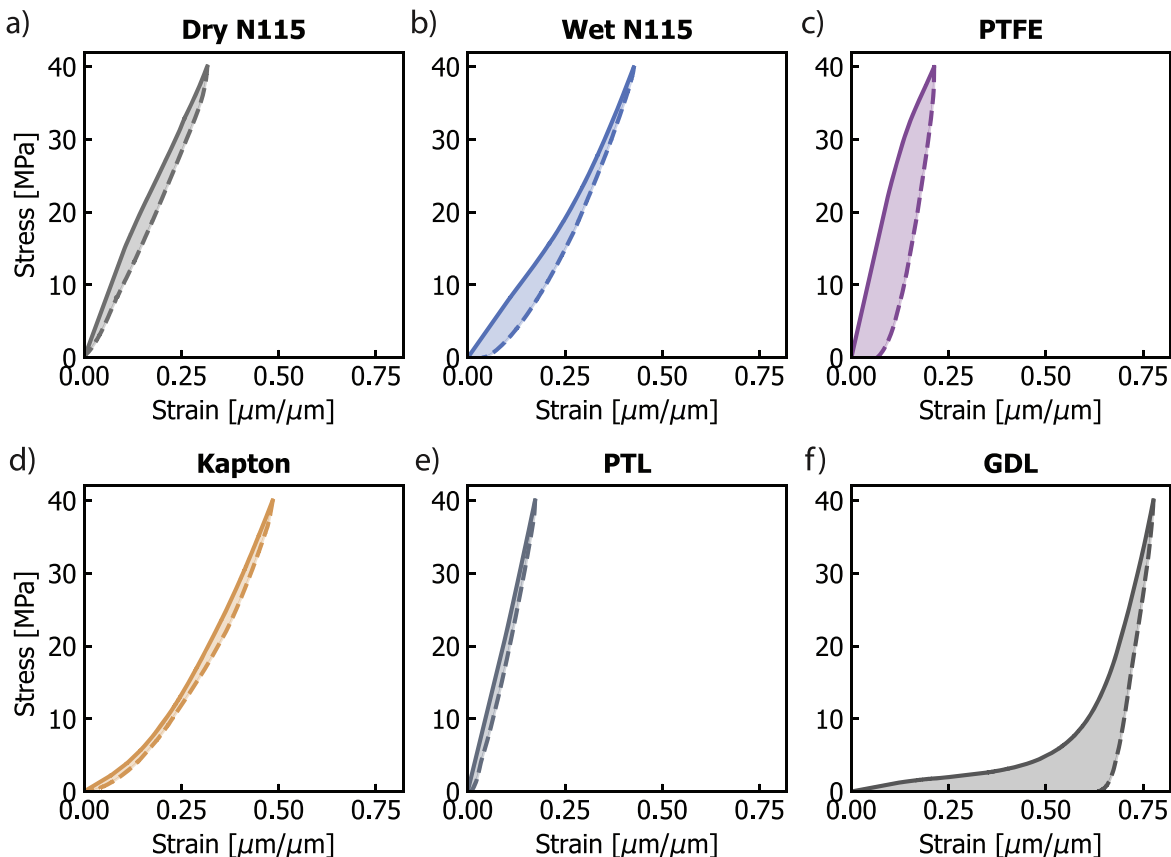


Figure 4. Load and unload stress-strain curves of components in compression regime at 25 °C: (a) Dry PFSA membrane, (b) Hydrated PFSA membrane, (c) PTFE, (d) Kapton, (e) PTL, (f) GDL. Loading curves are solid lines and unloading curves are dashed lines. The (shaded) area between the load-unload curves represents the mechanical energy the material dissipates under deformation.

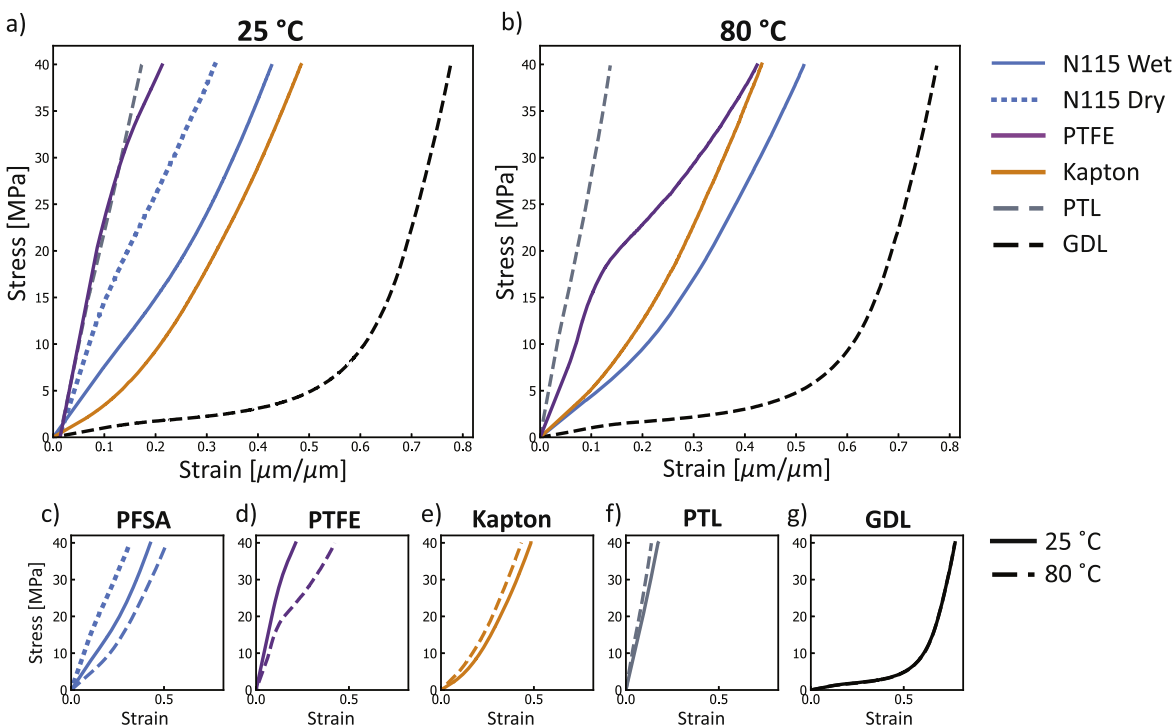


Figure 5. Engineering stress-strain curves of components in compression regime at (a) 25 °C and (b) 80 °C. Comparison of temperatures for individual materials: (c) Hydrated PFSA membrane (in water), (d) PTFE, (e) Kapton, (f) PTL, (g) GDL. Color coding of the materials is the same as used in Fig. 4.

40 MPa, PTFE reaches a compressive strain value of 25%, compared to 35 and 45% for dry and hydrated PFSA, respectively (Fig. 4c). However, PTFE has greater energy dissipation and slightly higher permanent strain than both dry and hydrated PFSA. Compared to PFSA, PTFE shows less sensitivity to temperature even though softening is observed at high stresses (Fig. 5). Kapton shows stronger thermal stability than PFSA and PTFE as evidenced by the close stress-strain curves at low and high temperatures which also have similar curvatures (Fig. 5). The load-unload curve of Kapton also shows lower energy dissipation but slightly higher permanent strain compared to PTFE (Fig. 4d).

The titanium fiber or felt PTL (Bekaert 2GDL10N) is a porous metal (56% nominal porosity) which exhibits linearity (Fig. 4e). By contrast, the GDL is a soft, porous material composed of carbon fibers which exhibits nonlinear compression behavior. The nonlinearity of the GDL is attributed to the collapse of pore structures leading to an increase in contact between fibers with compression and then an increase in stiffness (Fig. 4f).^{14,43–45,47} However, compared to PTL, there is greater deformation and damage in GDL as evidenced by the load-unload curve showing significant permanent strain as the sample (pore structure) is crushed, which was observed and analyzed in previous studies.^{46–49}

Mechanical properties of components.—A comparison of effective modulus, toughness, and energy dissipation of all components and between 25 and 80 °C is provided in Fig. 6. The calculation of the secant modulus is described in the SI. The stress-strain curve for PFSA becomes more nonlinear in water and at higher temperatures. Therefore, the linearization of the stress-strain curve for PFSA is not trivial, yet the values here provide a comparison point.

Among the polymeric materials, PFSA has the lowest secant modulus at elevated temperatures, followed by Kapton then PTFE. The effective modulus of PFSA decreases from 145 MPa in dry state at 25 °C to 45 MPa in water at 80 °C. PTFE softens with increased temperature, as evidenced by the secant modulus decreasing from 234 MPa to 152 MPa. Kapton has lower stiffness than PTFE with a secant modulus of 35 and 50 MPa for 25 and 80 °C, respectively. Lastly, among the porous materials, GDL's secant modulus of 7.8 MPa is two orders of magnitude smaller than PTL, which has a secant modulus of 280 MPa at 80 °C.

The toughness of the cell components is not affected by the temperature change, apart from PTFE. Wet PFSA exhibits an increase of toughness with increasing hydration (from 6.5 to 8.2 MJ/m³ for membrane in dry state at 25 °C to wet state at 80 °C, respectively) because it can accommodate more deformation owing to higher mobility of its constituent units, especially in hydrated state. The toughness values for PTFE indicate a temperature dependence as the toughness increases from 4.8 to 9.5 MJ/m³. Kapton is more thermally stable than PTFE and has a toughness of about 7 MJ/m³ at both temperatures. PTL has the lowest toughness (3.3 MJ/m³ at 80 °C) of the cell components due to its rigid porous structure that collapses under pressure. GDL, being a softer carbon-based porous material, has a greater toughness than PTL. The energy dissipation for PFSA and PTFE is larger at higher temperature likely due to higher chain mobility. The greater energy dissipation in GDL (~5.5 MJ/m³) is consistent with the larger permanent deformation resulting from the damage within the carbon fiber structure.^{21,47–49} The weaker temperature dependence of mechanical properties for Kapton, PTL, and GDL indicates greater thermal stability of these materials within this temperature range.

Dimensional and volumetric analysis.—In this section, the change in sample dimensions is analyzed to assess if a permanent volume change has occurred. The longitudinal, radial, and volumetric strains are calculated based on measurements of the sample dimensions (thickness and diameter) before and at the end of the compression experiment based on LVDT displacement measurements (Table II). Since polymers are viscoelastic, the final measurements are taken several minutes after load removal using the depth

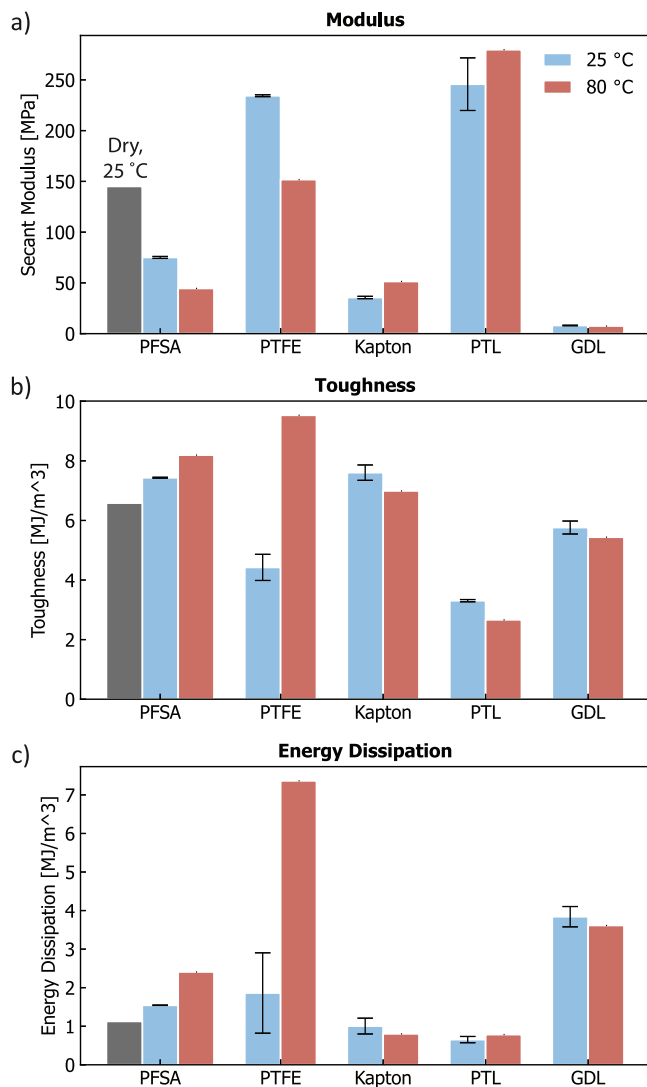


Figure 6. (a) Effective modulus of dry (gray, 25 °C) and wet PFSA, PTFE, Kapton, PTL, and GDL during uniaxial compression test at 25 (blue) and 80 °C (red). (b) Toughness and (c) energy dissipated during compression test. Error bars represent the standard deviation.

probe. A change in dimensions upon load removal (non-zero strain) indicates a permanent deformation. For a cylindrical sample in radial coordinates, the plastic volumetric strain, ϵ_v^p , is given by:

$$\epsilon_v^p = \epsilon_z^p + 2\epsilon_r^p \quad [7]$$

where ϵ_z^p is the permanent longitudinal (thickness) strain and ϵ_r^p is the plastic radial (in-plane) strain.

At 25 °C, the PFSA membrane has permanent dimensional change in two directions yet exhibits a near-zero volume change (Table II). Thus, PFSA membranes compressed to 40 MPa exhibit permanent thickness reduction ($\epsilon_z^p < 0$) while expanding in the plane ($\epsilon_r^p < 0$) with an overall net volume change of near zero due to incompressible plastic deformation. A similar response is observed for PTFE and Kapton, the other polymeric materials studied herein. Wet PFSA exhibits greater volume change which could be attributed to water leaving the polymer matrix.²²

For porous materials (GDL and PTL), there is a permanent volume change as their micro-porous morphology are compressed resulting in a reduced porosity ($\epsilon_v^p < 0$). This deformation mechanism is different from PFSA, or solid incompressible materials, in that porous materials show negligible permanent radial strain compared to longitudinal

Table II. Permanent strains under compression calculated based on measurements of samples taken before and after the compression test (outside of compression apparatus).^{a)}

Material	RH %	Temperature °C	Permanent thickness strain ε_z^p	Permanent radial (in-plane) strain ε_r^p	Permanent volumetric strain ε_v^p	Notes on nature of material
N115	100	25	-1.4%	1.7%	2.0%	Solid ionomer in liquid water
N115	50	25	-0.1%	0.4%	0.7%	Solid ionomer in air (50%RH)
PTFE	42	25	-2.4%	1.8%	1.3%	Solid polymer
Kapton	41	25	-1.0%	0.8%	1.0%	Solid polymer
PTL	46	25	-11.5%	0.3%	-10.9%	Porous metal
GDL	43	25	-64.0%	5.3%	-32.0%	Soft, porous material

a) The values at higher temperatures are conflated with the thermal expansion and contraction during the experiments and therefore omitted from the analysis.

strain due to thickness contraction. In essence, the porous materials do not expand in-plane when compressed in thickness direction, which result in collapse of their porous-finer structure as also reported in previous studies.^{21,47,49} Therefore, a constant volume assumption is not applicable to porous materials.

Constitutive modeling of PFSA.—As mentioned previously, PFSA's mechanical response alters with hydration and temperature which is observed as increased water uptake at elevated temperatures, as shown in Hydration State in Membrane section. With an increase in temperature from 25 °C to 80 °C, PFSA undergoes softening and greater strain (thickness reduction) is observed under the same stress (Fig. 7). As noted previously, the stress-strain response is nonlinear for PFSA, therefore, a standard Young's modulus is not evident from these curves. Thus, an instantaneous stiffness is defined from the tangent modulus, E_z , which is the derivative of the stress-strain curve (Fig. 7). Figure 7d shows that at 80 °C instantaneous modulus, E_z , shows a linear dependence on the strain, which can be expressed as:

$$E_z = \frac{d\sigma}{d\varepsilon} = C\varepsilon \quad [8]$$

Integrating this expression gives:

$$\int d\sigma = \int C\varepsilon d\varepsilon \quad [9]$$

$$\sigma = \frac{1}{2}C\varepsilon^2 \quad [10]$$

where C is the slope of the tangent modulus vs strain curve in Fig. 7d which equals to 242 MPa (best-fit to 80 °C data). This expression is similar to a power law function describing strain hardening during plastic deformation. However, the contribution of plasticity is not described by this expression.

While Eq. 10 captures the compressive stress-strain response, this is only accomplished at 80 °C and in liquid water. Another approach using hyperelastic constitutive models can describe the nonlinear stress-strain response of PFSA for a wider scope of environmental conditions. Inspired by the hydration-driven mobility and elastomeric behavior, we adopt rubber elasticity theories to reproduce the experimental data. Even though there is an indication for permanent deformation in PFSA under high compressive stresses, the stress-strain curve of hydrated membrane exhibits rubbery behavior without a discernible linear elastic region.

Hyperelastic material models are a class of constitutive models that were first introduced to describe incompressible, rubber elastomers where the stress-strain relationship is derived from the strain energy density function, W .^{66,67} A reduced form of the polynomial hyperelasticity model is given by.⁶⁸

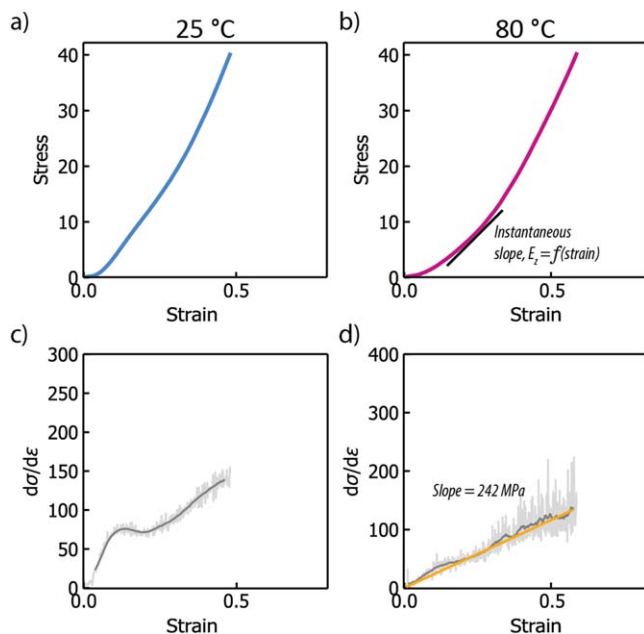


Figure 7. (a)–(b) Hydrated PFSA (N115 AsR) engineering stress strain curve at 25 and 80 °C. (c-d) Derivative of stress strain curves (tangent modulus, E_z) vs engineering strain.

$$W = \sum_{i=0}^n C_{i0}(I_1 - 3)^i \quad [11]$$

where $I_1 = \lambda_1^2 + \lambda_2^2 + \lambda_3^2 = \lambda^2 + 2\lambda^{-1}$ and $\lambda_{i=1,2,3}$ are the principal stretches and in the uniaxial case stretch is defined to be:

$$\lambda = 1 + \varepsilon_{eng} \quad [12]$$

The stress tensor can be found by taking the derivative of the strain energy function with respect to the strain. For $n=1$, the polynomial strain energy function is reduced to the neo-Hookean model. The nominal stress-stretch relation for the neo-Hookean model in uniaxial deformation simplifies to:

$$\sigma_{11} = C_{10} \left(\lambda - \frac{1}{\lambda^2} \right) \quad [13]$$

where $C_{10} = \frac{\mu}{2}$ and μ is the initial shear modulus.

Figure 8 compares the experimental stress-strain curves of PFSA with the neo-Hookean model using best-fit parameters as tabulated in Table III. The model generally captures the mechanical response

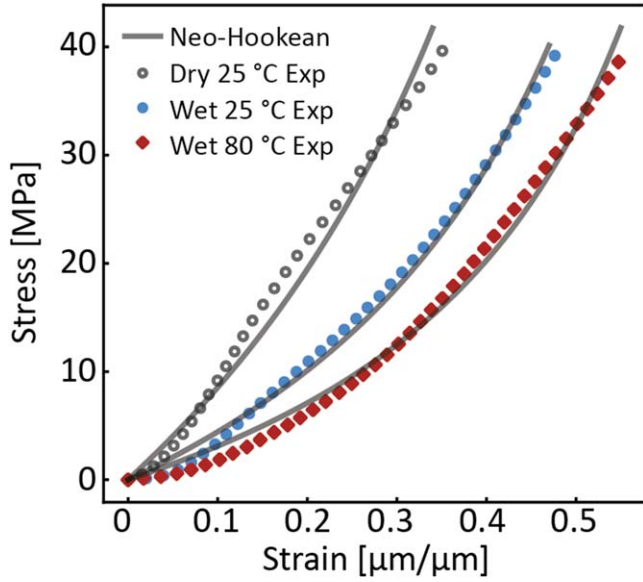


Figure 8. PFSA experimental data vs model dry (25 °C) and hydrated (25 and 80 °C).

Table III. Model fitting parameters for neo-Hookean model.

Temperature °C	RH %	C ₁₀ MPa	R2
25	50 (ambient)	25.51	0.9775
25	100 (liquid water)	13.25	0.9942
80	100 (liquid water)	9.31	0.9913

well in all conditions, even though the agreement improves at high temperature and hydration. PFSA membrane's tensile response was shown to transition from a semi-crystalline response to gel-like behavior in liquid water, as reported by Kusoglu et al.²⁸ However, the neo-Hookean model does not capture the behavior well in lower hydration state.

Mechanics of assembly compression: 1D spring-network model.—To predict the compression of the electrolyzer cell components, a 1D spring network model is developed using the measured mechanical properties. The simplified network consists of a spring element for each component which are arranged in series or parallel to represent the cell assembly (Fig. 9). In this simplified version of a standard assembly, a PFSA membrane (without catalyst layers) is sandwiched between the PTL and the GDL with PTFE gaskets at both edges. Therefore, the PTFE gasket and PTL are in parallel forming *Group A* at the anode side. Similarly, PTFE and GDL form *Group C* at the cathode side. Those two groups are in series with the Grade 2 Titanium (Ti) flow plates and the PFSA membrane.

Each spring element is then assigned a compressive stiffness (E_i) determined from the experimental data discussed above. When the entire assembly is deformed under an applied stress, $\sigma_{applied}$, (compressive stress) the strain of each spring component undergoing the same stress can be calculated as follows:

$$\sigma_{applied} = E_i \varepsilon_i \quad [14]$$

where E_i , ε_i is the stiffness and strain, respectively, in each component, i .

For PFSA, a modified spring element with an adaptive modulus is implemented based on the nonlinear stress-strain response observed (Fig. 7). The adaptive modulus increases proportionally

as the material is strained under compression exhibiting increasing stiffness. The stress-strain expression from Eq. 10 is implemented for the compressive response of PFSA at 80 °C. Therefore, for PFSA, $E_{PFSA} = \frac{1}{2} C \varepsilon_{PFSA}$. Thus, the compressive strain as a function of applied stress is:

$$\varepsilon_{PFSA} = \sqrt{\frac{\sigma}{\frac{1}{2}C}} \quad [15]$$

The strain of the components in parallel are equivalent such that:

$$\varepsilon_A = \varepsilon_{PTFE}^A = \varepsilon_{PTL} \varepsilon_C = \varepsilon_{PTFE}^C = \varepsilon_{GDL} \quad [16]$$

Within each group, the porous layers cover the active area while the gasket covers the inactive area. The total force is applied between the two areas such that:

$$F = F_{active} + F_{gasket} \quad [17]$$

The distribution of stress between the components is expressed as:

$$\sigma = \frac{F}{A_{total}} = \frac{F_{active}}{A_{active}} \frac{A_{active}}{A_{total}} + \frac{F_{gasket}}{A_{gasket}} \frac{A_{gasket}}{A_{total}} \quad [18]$$

Letting f_{aa} be the fraction of active area, the stresses are distributed to the two groups such that:

$$\begin{aligned} \sigma_A &= \sigma_{PTFE}^A (1 - f_{aa}) + \sigma_{PTL} f_{aa}, \\ \sigma_C &= \sigma_{PTFE}^C (1 - f_{aa}) + \sigma_{GDL} f_{aa}. \end{aligned} \quad [19]$$

The stress in the components in series are equivalent along the network:

$$\sigma_{applied} = \sigma_{Ti} = \sigma_A = \sigma_{PFSA} = \sigma_C. \quad [20]$$

Therefore, the strain in *Group A* (anode side) is related to stress such that:

$$\varepsilon_A = \frac{\sigma_{applied}}{E_{PTFE}(1 - f_{aa}) + E_{PTL} f_{aa}}. \quad [21]$$

The strain in *Group C* (cathode side) is given by:

$$\varepsilon_C = \frac{\sigma_{applied}}{E_{PTFE}(1 - f_{aa}) + E_{GDL} f_{aa}}. \quad [22]$$

The total strain (thickness changes) of the network assembly is the sum of the strains in the individual elements normalized by the total thickness of the cell, L , connected in series:

$$\varepsilon_{Total} = \varepsilon_{Ti} \frac{L_{Ti}}{L} + \varepsilon_A \frac{L_A}{L} + \varepsilon_{PFSA} \frac{L_{PFSA}}{L} + \varepsilon_C \frac{L_C}{L}. \quad [23]$$

By solving this system of equations, the strains of components can be determined as a function of applied stress. Figure 10 shows the strains of components at 5, 10, and 20 MPa stress from the experimental data compared with strains estimated from the simplified cell assembly representation. In each sub element with two parallel components, the stiffer component carries more of the stress and dominates the equivalent strain in the element. Thus, to represent *Group A*, the experimental strain value from the PTL is used because the PTFE has a lower stiffness than PTL. Similarly, PTFE is representative of *Group C* since PTFE (152 MPa) is significantly stiffer than the GDL (7.8 MPa). GDL is thicker than PTFE, but its thickness will reduce to that of PTFE during initial assembly which will generate a small initial strain, which is ignored due to its low stiffness. Thus, the deformation of *Group C* is determined predominantly by PTFE since it is stiffer than GDL in the strain regime modeled. Conversely, the deformation of the

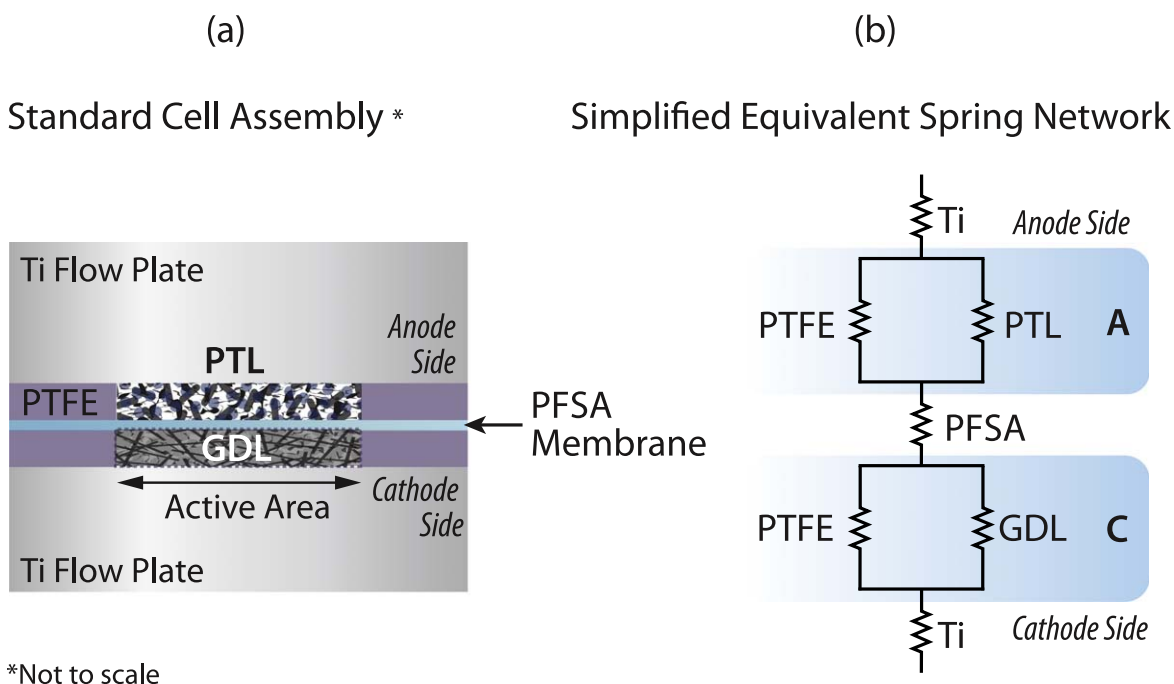


Figure 9. (a) Simplified schematic of a standard electrolyzer assembly and (b) a representative equivalent spring model of the cell assembly.

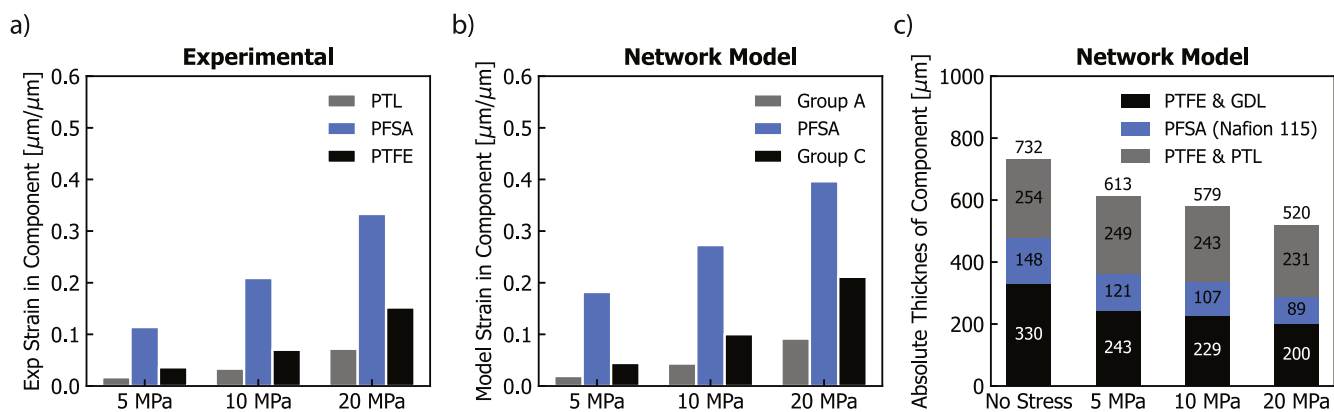


Figure 10. (a) Experimental strain measurements from uniaxial compression of individual components. PTL is representative of the displacement in *Group A* from the model and PTFE is representative of *Group C* since PTFE does the majority of load bearing as illustrated in the SI. (b) Strains in *Group A*, PFSA, and *Group C* are calculated from the 1D model. (c) Absolute thickness of components when modeled in the 1D network based on experimental data and a 25 cm² active area cell.⁶⁹

titanium flow plate remains elastic with negligible strain because its modulus of elasticity or Young's modulus is three orders of magnitude greater than the stiffest components in the cell, and therefore, it can be neglected and is not represented in the plot.

Using the stiffness values from the experimental data (Table IV) and assuming a cell with an active area of 25 cm² (based on a cell design from NREL⁶⁹), the thickness change in each component under applied pressure (of 0, 5, 10, and 20 MPa) are summarized in Fig. 10. The electrolyzer assembly is represented mechanically by three dominant components stacked together with an initial total thickness of 732 μm (Fig. 10). As this system is compressed, the total thickness decreases with different contributions from each component based on their stiffness. The change of this relative strain contribution as a function of applied stress can be seen in Fig. S7d. At low compression levels, PFSA (Nafion 115) membrane contributes most to the thickness reduction, followed by *Group C*, then *Group A*. For example, at 10 MPa, the total assembly thickness decreases by 153 μm to 579 μm , with the greatest contribution coming from the Nafion 115 membrane (~53% of total thickness

change). Meanwhile, *Group C* and *A* contribute 34 and 15%, respectively. At higher compression levels, the membrane becomes stiffer with strain hardening, which reduces the rate of additional thickness reduction. Therefore, with compressions over 20 MPa, *Group C* contributes a greater percentage of thickness reduction than does the PFSA membrane. *Group A*'s contribution to thickness reduction, however, remains under 20% due to their greater stiffness. For example, under 40 MPa compression, PFSA membrane accounts for 34% of the thickness reduction while *Group C* and *A* account for 45 and 20%, respectively.

Figure S7 in the SI compares the percent of total thickness change for varying cell sizes. Tables S2 and S3 list the 6 cells compared and their active and total areas and the active area fraction (from 0.13 to 0.6). With increasing active area fraction, *Group C* (cathode side) contributes more to the total thickness reduction while *Group A* (anode side) contribution decreases. This is because the gasket area fraction decreases with increasing active area fraction, thereby increasing the stress field in the PTFE and reducing the cathode side thickness further (especially when in parallel with the

Table IV. Modulus values calculated from experimental data (except Ti) used in the 1D spring network model of electrolyzer cell. The parameter C = 242 MPa.

Material	Thickness	Modulus definition (80 °C) [MPa]	Notes and references
Nafion 115 Wet	147 μm	$\frac{1}{2}C\epsilon_{\text{PFSA}}$	Strain-dependent
Bekaert 2GDL10N	254 μm	280	
Skived PTFE	254 μm	152	
MGL280	330 μm	7.8	
Grade II Ti	1 inch (25400 μm)	110,000	From Ref. 70
PTL + Nafion + GDL	732 μm	N/A	

softer GDL). In *Group A*, however, the PTL carries more of the stress load as the active area fraction increases thereby resulting in a lesser thickness reduction.

Due to the linearization of the deformation in the components (except PFSA), the strain calculated from the model (Fig. S7b) is slightly greater compared with the experimental values at lower stresses (5 and 10 MPa) (Fig. 10a). In addition, at higher loadings, it would be expected that the PTFE gasket on the cathode side would yield as the stress in this component would exceed the elastic limit at 80 °C. Despite the simplification of the approach, the model provides a comparative analysis of thickness change of an electrolyzer assembly under compression (Fig. 10b). The model captures the nonlinear deformation of the PFSA well, due to the modified stress-strain relationship used (Fig. S6c). The other cell components have a linear response, albeit with permanent deformation occurring particularly in porous materials (Fig. S6). Thus, this model could be interpreted as a first order approximation of the compression of an electrolyzer cell even though in reality there is a distribution of thicknesses across the MEA and components with nonlinear effects^{15,55} as well as time-dependent changes in the form of creep as evidenced for membranes³³ which however cannot easily be applied to porous components. Nevertheless, this study focuses on the comparative analysis of compressive mechanical response of cell components provides guidance for their relative thickness change under pressure and underscores the role of gasket elements in redistributing the stress load. The results reported herein would benefit studies focusing on cell assembly strategies as well as investigations focusing on mechanical durability of electrolyzer membranes and stability of their interfaces with the electrodes and PTLs.^{6,8,9,17,55}

Conclusions

This study investigates the mechanical response of electrolyzer cell components under quasistatic compression in device-relevant environmental conditions. All electrolyzer cell components were tested in uniaxial compression at 25 and 80 °C, from which several compressive mechanical properties are extracted. The permanent deformation of each component was examined from the analysis of the loading-unloading curves. Based on the notion of increased mobility of polymer chains under hydration and higher temperatures, an elastomer mechanics constitutive model was adopted to reproduce the compressive response of PFSA (Nafion 115 membrane). The hyperelastic constitutive model of PFSA provides a benchmark for prediction purposes and can be extended to complex loading where experiments are impractical. The collected data were also used to develop a 1D spring network model to analyze the thickness reduction of an electrolyzer cell under compressive load.

The compressive stress-strain responses of most electrolyzer cell components have a degree of nonlinearity owing to the unique morphologies and deformation mechanisms of each component. The elevated temperature had a minimal impact on the stress-strain response of the GDL, PTL, and Kapton but had a noticeable softening effect in PFSA and PTFE. Additionally, PFSA membrane's compressive response exhibited an increasing degree of nonlinearity and softening with increasing water content (from dry to

liquid water). Using the expression for the nonlinear response of PFSA and the linearized response of other electrolyzer cell components at 80 °C, a 1D spring network model representative of a cell assembly was developed to predict the thickness changes of components' applied stress and can be easily adapted to assess the effect of changing the active area relative to the total area or gasketed area.


This study elucidates the mechanical response of solid polymers and porous metal or carbon fiber cell components under compression at low and elevated temperatures and provides a qualitative comparison of their deformation behavior and quantitative analysis of their thickness change and mechanical properties. This work improves understanding of compression-induced mechanical interactions between membrane and cell components and can help assess material design and assembly strategies for improved durability.

Acknowledgments

This work was carried out under HydroGEN and H2NEW consortia, funded by the Hydrogen and Fuel Cell Technologies Office (HCTO), of the Office of the Energy Efficiency and Renewable Energy (EERE), of the U.S. Department of Energy under contract number DE AC02-05CH11231. We thank the Energy Conversion Group and the Ionomer Group at LBNL. We thank Jacob Wrubel (NREL) for insightful discussions. We thank Aiden Brutman (UC Berkeley) for assistance in collecting experimental data. We thank Dr. Douglas Kushner for fruitful discussions and insights during data analysis and interpretation.

ORCID

Claire Arthurs  <https://orcid.org/0000-0002-9150-8349>

Ahmet Kusoglu  <https://orcid.org/0000-0002-2761-1050>

References

- IEA, *Global Hydrogen Review 2023 Licence: CC BY 4.0*, IEA, Paris (2023).
- Technical Targets for Proton Exchange Membrane Electrolysis DOE Hydrogen and Fuel Cell Technologies Office (2023).
- K. A.-D. Ayers, Luke, A. Roemer, B. Carter, M. Niedzwiecki, J. Manco, E. Anderson, C. Capuano, C.-Y. Wang, and Z. Wei, *High performance, low cost hydrogen generation from renewable energy RPT1801*, USDOE Office of Energy Efficiency and Renewable Energy (EERE) (2014).
- A. Buttler and H. Spliethoff, *Renew. Sustain. Energy Rev.*, **82**, 2440 (2018).
- B. Pivovar, *H2NEW: Hydrogen (H2) from Next-generation Electrolyzers of Water Overview*, U.S. Department of Energy Hydrogen Program's 2023 Annual Merit Review and Peer Evaluation Meeting (Washington, DC) (2023).
- K. Ayers, *Curr. Opin. Chem. Eng.*, **33**, 100719 (2021).
- T. T. Phan, S. K. Kim, J. Islam, M. J. Kim, and J. H. Lee, *Int. J. Hydrogen Energy*, **49**, 875 (2024).
- K. Ayers, N. Danilovic, R. Ouimet, M. Carmo, B. Pivovar, and M. Bornstein, *Annu. Rev. Chem. Biomol.*, **10**, 219 (2019).
- E. J. Park, C. G. Arges, H. Xu, and Y. S. Kim, *ACS Energy Lett.*, **7**, 3447 (2022).
- K. Ayers, N. Danilovic, K. Harrison, and H. Xu, *Electrochem. Soc. Int.*, **30**, 67 (2021).
- S. Stucki, G. G. Scherer, S. Schlagowski, and E. Fischer, *J. Appl. Electrochem.*, **28**, 1041 (1998).
- P. Millet, A. Ranjbari, F. de Guglielmo, S. A. Grigoriev, and F. Auprêtre, *Int. J. Hydrogen Energy*, **37**, 17478 (2012).
- S. A. Grigoriev, K. A. Dzhush, D. G. Bessarabov, and P. Millet, *Int. J. Hydrogen Energy*, **39**, 20440 (2014).
- X. Q. Xing, K. W. Lum, H. J. Poh, and Y. L. Wu, *J. Power Sources*, **195**, 62 (2010).

15. S. Garbe, J. Futter, A. Agarwal, M. Tarik, A. A. Mularczyk, T. J. Schmidt, and L. Gubler, *J. Electrochem. Soc.*, **168**, 044515 (2021).
16. Y. H. Chen, C. F. Liu, J. C. Xu, C. F. Xia, P. Wang, B. Y. Xia, Y. Yan, and X. Y. Wang, *Small Struct.*, **4**, 1 2200130 (2023).
17. M. Carmo, D. L. Fritz, J. Merge, and D. Stolten, *Int J Hydrogen Energ.*, **38**, 4901 (2013).
18. X. T. Wang, Y. Song, and B. Zhang, *J. Power Sources*, **179**, 305 (2008).
19. A. Kusoglu, A. M. Karlsson, M. H. Santare, S. Cleghorn, and W. B. Johnson, *J. Power Sources*, **161**, 987 (2006).
20. R. Jiang, C. K. Mittelsteadt, and C. S. Gittleman, *J. Electrochem. Soc.*, **156**, B1440 (2009).
21. S. G. Kandlikar, Z. Lu, T. Y. Lin, D. Cooke, and M. Daino, *J. Power Sources*, **194**, 328 (2009).
22. A. Kusoglu, B. L. Kienitz, and A. Z. Weber, *J. Electrochem. Soc.*, **158**, B1504 (2011).
23. T. Uchiyama, M. Kato, and T. Yoshida, *J. Power Sources*, **206**, 37 (2012).
24. A. Kusoglu and A. Z. Weber, *Chem. Rev.*, **117**, 987 (2017).
25. N. B. Danilovic, G. Bender, and A. Weber, *H2NEW Hydrogen (H2) from Next-generation Electrolyzers of Water: H2NEW LTE: Performance and Benchmarking, 2021 Annual Merit Review and Peer Evaluation Meeting* (Washington, DC) (2021).
26. C. Feng, Y. Li, K. N. Qu, Z. M. Zhang, and P. F. He, *RSC Adv.*, **9**, 9594 (2019).
27. Y. L. Tang, A. M. Karlsson, M. H. Santare, M. Gilbert, S. Cleghorn, and W. B. Johnson, *Mat. Sci. Eng. a-Struct.*, **425**, 297 (2006).
28. A. Kusoglu, Y. L. Tang, M. Lugo, A. M. Karlsson, M. H. Santare, S. Cleghorn, and W. B. Johnson, *J. Power Sources*, **195**, 483–492 (2010).
29. A. Kusoglu, Y. L. Tang, M. H. Santare, A. M. Karlsson, S. Cleghorn, and W. B. Johnson, *J. Fuel Cell Sci. Tech.*, **6** (2009).
30. M. N. Silberstein and M. C. Boyce, *J. Power Sources*, **195**, 5692 (2010).
31. S. Shi, Z. Liu, Q. Lin, X. Chen, and A. Kusoglu, *Soft Matter*, **16**, 1653 (2020).
32. A. Kusoglu, A. Hexemer, R. C. Jiang, C. S. Gittleman, and A. Z. Weber, *J. Membrane Sci.*, **421**, 283 (2012).
33. C. Arthurs and A. Kusoglu, *ACS Appl. Energy Mater.*, **4**, 3249 (2021).
34. A. Martin, P. Trinke, M. Stähler, A. Stähler, F. Scheepers, B. Bensmann, M. Carmo, W. Lehnert, and R. Hanke-Rauschenbach, *J. Electrochem. Soc.*, **169**, 014502 (2022).
35. J. S. Bergström and L. B. Hilbert, *Mech. Mater.*, **37**, 899 (2005).
36. J. L. Jordan, C. R. Siviour, J. R. Foley, and E. N. Brown, *Polymer*, **48**, 4184 (2007).
37. S. C. Khatua and S. Maiti, *Eur. Polym. J.*, **38**, 537 (2002).
38. C. T. Kuo, M. C. Yip, K. N. Chiang, and C. Tsou, *J. Electron. Mater.*, **34**, 272 (2005).
39. J. B. Ge, A. Higier, and H. T. Liu, *J. Power Sources*, **159**, 922 (2006).
40. A. El-kharouf and R. Steinberger-Wilckens, *Fuel Cells*, **15**, 802 (2015).
41. R. W. Atkinson, Y. Garsany, B. D. Gould, K. E. Swider-Lyons, and I. V. Zenyuk, *ACS Appl. Energy Mater.*, **1**, 191 (2018).
42. N. Kulkarni, J. I.-S. Cho, R. Jervis, E. P.-L. Roberts, I. Francesco, M. D.-R. Kok, P. R. Shearing, and D. J.-L. Brett, *J. Power Sources*, **521**, 230973 (2022).
43. C. Carral and P. Mélé, *Int. J. Hydrogen Energ.*, **43**, 19721 (2018).
44. M. Ouerghemmi, C. Carral, and P. Mele, *J. Electrochem. Soc.*, **170**, 104508 (2023).
45. T. Le Carre, J. F. Blachot, J. P. Poirot-Crouvezier, and J. Laurencin, *Int. J. Hydrogen Energ.*, **50**, 234 (2024).
46. S. Escibano, J. F. Blachot, M. Ethève, A. Morin, and R. Mosdale, *J. Power Sources*, **156**, 8 (2006).
47. A. Bazylak, D. Sinton, Z. S. Liu, and N. Djilali, *J. Power Sources*, **163**, 784 (2007).
48. W. R. Chang, J. J. Hwang, F. B. Weng, and S. H. Chan, *J. Power Sources*, **166**, 149 (2007).
49. V. Norouzfard and M. Bahrami, *J. Power Sources*, **264**, 92 (2014).
50. E. Borgardt, O. Panchenko, F. J. Hackemüller, J. Giffin, M. Bram, M. Müller, W. Lehnert, and D. Stolten, *J. Power Sources*, **374**, 84 (2018).
51. F. J. Hackemüller, E. Borgardt, O. Panchenko, M. Müller, and M. Bram, *Adv. Eng. Mater.*, **21**, 1801201 (2019).
52. Y. H. Chen, J. E. Frith, A. Dehghan-Manshadi, H. Attar, D. Kent, N. D.-M. Soro, M. J. Birmingham, and M. S. Dargusch, *J. Mech. Behav. Biomed.*, **75**, 169 (2017).
53. B. R. Wang, T. Sun, K. Fezzaa, J. Y. Huang, and S. N. Luo, *Mater. Lett.*, **245**, 134 (2019).
54. G. Liu, W. D. Song, and P. F. Li, *Compos. Struct.*, **233**, 111703 (2020).
55. A. Martin, P. Trinke, M. Stähler, A. Stähler, F. Scheepers, B. Bensmann, M. Carmo, W. Lehnert, and R. Hanke-Rauschenbach, *J. Electrochem. Soc.*, **169**, 014502 (2022).
56. E. Leonard, A. D. Shum, N. Danilovic, C. Capuano, K. E. Ayers, L. M. Pant, A. Z. Weber, X. H. Xiao, D. Y. Parkinson, and I. V. Zenyuk, *Sustain. Energ. Fuels*, **4**, 921 (2020).
57. E. Hoppe, S. Holtwerth, M. Müller, and W. Lehnert, *J. Power Sources*, **578** (2023).
58. Chemours, *Nafion Membranes—The Right Choice for Your Flow Battery Technology Product Overview*, The Chemours Company FC, LLC (2017).
59. AvCarb® MGL Carbon Papers for Gas Diffusion Layers, AvCarb Material Solutions (2021).
60. M. K. Budinski and A. Cook, *Tsinghua Science & Technology*, **15**, 385 (2010).
61. A. Kusoglu, Y. L. Tang, M. H. Santare, A. M. Karlsson, S. Cleghorn, and W. B. Johnson, *J. Fuel Cell Sci. Technol.*, **6**, 011012 (2009).
62. Y. S. Kim, L. M. Dong, M. A. Hickner, T. E. Glass, V. Webb, and J. E. McGrath, *Macromolecules*, **36**, 6281 (2003).
63. D. Liu, S. Kyriakides, S. W. Case, J. J. Lesko, Y. X. Li, and J. E. McGrath, *J. Polym. Sci. Pol. Phys.*, **44**, 1453 (2006).
64. P. J. Rae and D. M. Dattelbaum, *Polymer*, **45**, 7615 (2004).
65. E. N. Brown, P. J. Rae, D. M. Dattelbaum, B. Clausen, and D. W. Brown, *Exp. Mech.*, **48**, 119 (2008).
66. M. Mooney, *J. Appl. Phys.*, **11**, 582 (1940).
67. L. R.-G. Treloar, *T Faraday Soc.*, **39**, 241 (1943).
68. R. W. Ogden, *Non-linear Elastic Deformation* (Dover Publications, Inc., Mineola, New York) (1984).
69. J. Wrubel, S. Ware, C. Schaffer, M. Allen, E. Klein, R. Rice, C. Engtrakul, and G. Bender, "NREL 25-cm² High-Pressure Low-Temperature Electrolysis Cell Hardware (Open Source)." *NREL Data Catalog* (2023).
70. Titanium Grade 2 (2024), ASM Material Data Sheet MatWeb, LLC.